On the Scale Interactions that Dominate the Maintenance of a Persistent Heavy Rainfall Event: A Piecewise Energy Analysis

SHEN-MING FU

International Center for Climate and Environment Sciences, Institute of Atmospheric Physics, Chinese Academy of Sciences, Beijing, China

RUI-XIN LIU

Laboratory of Cloud–Precipitation Physics and Severe Storms, Institute of Atmospheric Physics, Chinese Academy of Sciences, Beijing, China

JIAN-HUA SUN

Laboratory of Cloud–Precipitation Physics and Severe Storms, Institute of Atmospheric Physics, Chinese Academy of Sciences, and State Key Laboratory of Severe Weather, Chinese Academy of Meteorological Sciences, Beijing, China

(Manuscript received 8 October 2017, in final form 4 December 2017)

ABSTRACT

Persistent heavy rainfall events (PHREs) are the product of the combined effects of multiscale systems. A PHRE that occurred during the 2016 mei-yu season was selected to further the understanding of the scale interactions accounting for the persistence of this type of event. The scale interactions were analyzed quantitatively using a piecewise energy budget based on temporal scale separation. Results show that the strongest interactions between the precipitation-related eddy flow and its background circulation (BC) occur in the mid- to lower troposphere, where a significant downscale kinetic energy (KE) cascade alone dominates eddy flow persistence. An obvious upscale KE cascade (i.e., a feedback effect) appears in the mid- to upper troposphere but has a negligible effect on the BC. Overall, within the precipitation region, the downscale KE cascade is primarily dependent on BC signals with shorter periods, whereas the upscale KE cascade is more dependent on BC signals with longer periods. Thus, the BC has asymmetric effects on the KE cascades. The most significant BC signal as determined via wavelet analysis [i.e., quasi-biweekly (10–18 days) oscillations in this event] does not play the leading role in the downscale KE cascade. Instead, the quasi-weekly oscillations provide the maximum amount of energy for eddy flow maintenance. Semi-idealized simulations of various BC signals show similar results: precipitation and the intensities of lower-level shear lines and transversal troughs (both of which are closely related to the precipitation-related eddy flow) are more sensitive to the quasi-weekly oscillation than to the quasi-biweekly oscillation.

1. Introduction

In many regions around the world, heavy rainfall events are among the most frequent and severe meteorological disasters (Tao 1980; Karl and Knight 1998; Zhao et al. 2004; Schumacher and Johnson 2006; Davis and Lee 2012; Hitchens et al. 2013; Wang and Tan 2014; Fu et al. 2015; Liu and Wu 2016; Liu et al. 2016; Yamada et al. 2016). Heavy rainfall durations can vary from several minutes to several days (Tao 1980; Markowski and Richardson 2010; Li et al. 2015). A strong precipitation event with a relatively long lifetime (e.g., lasting for several days) that meets specific standards (e.g., Karl and Knight 1998; Bao 2007; Chen and Zhai 2015; Wang et al. 2014) can be defined as a persistent heavy rainfall event (PHRE).[1]

[1] In China, if the 24-h accumulated precipitation of a rainfall event exceeds 50 mm, it is regarded as a heavy rainfall event (Tao 1980). The definitions of a PHRE are different among different studies; for instance, Wang et al. (2014) defined three necessary conditions for a PHRE: (i) it covers a region larger than the lower limit of a meso-α-scale system (~200 km); (ii) precipitation meeting the standard of a heavy rainfall lasts for at least 5 days; and (iii) the overlapping rate of the rainbands in two continuous days exceeds 20%.

Corresponding author: Shen-Ming Fu, fusm@mail.iap.ac.cn

DOI: 10.1175/JAS-D-17-0294.1

Compared to shorter heavy rainfall events, PHREs tend to cause more severe flash flooding, urban waterlogging, and landslides. This results in larger economic losses and more substantial casualties. Therefore, significant efforts have been made to understand the conditions and mechanisms that lead to PHREs. Based on the previous studies, this study will investigate the mechanisms accounting for the maintenance of a PHRE from a viewpoint of scale interactions.

Favorable large-scale background circulation (BC) is confirmed to be crucial to PHRE occurrence. For instance, Tao (1980), Ding (1993), Zhao et al. (2004), and Bao (2007) have analyzed PHREs over central–eastern China and found that a long-lived quasi-stable large-scale BC, which features one or two strong blocking highs in the mid- to high latitudes and an intense western Pacific subtropical high (WPSH) in the lower latitudes, is a key condition for development of these PHREs. The long-lived blocking high continuously steers cold/dry air from the mid- to high latitudes to the lower latitudes, while the quasi-stationary western Pacific subtropical highs steer warm/moist air from the mid- to low latitudes to the higher latitudes (Wang et al. 2014; Chen and Zhai 2015). These two air flows with contrasting properties encounter each other continuously in the precipitation region, producing PHREs.

Scale interaction during PHREs is remarkable (Zhao et al. 2004; Fu et al. 2015; Zhang et al. 2016), which makes it an important way of understanding these types of events. The relevant studies can be roughly divided into two categories. Category 1 mainly includes those studies that qualitatively analyze the effects of various BC signals on maintaining a favorable precipitation configuration. For example, Yang and Li (2003) and Mao and Wu (2006) analyzed PHREs during the mei-yu season and suggested that intraseasonal oscillations favor them by forming upper-level anticyclonic anomalies and lower-level cyclonic anomalous circulation. Li et al. (2014) conducted wavelet analyses and composite studies on PHREs over the Yangtze River basin during the summer of 1996 and found that 30–60- and 10–25-day oscillations provide anomalous lower-level convergences that contribute to the PHREs. Liu et al. (2014) applied a bandpass filter to five PHREs during the 2003 mei-yu season and proposed that the quasi-biweekly oscillation (QBO) is crucial to these PHREs because it contributes southwesterly anomalies to the mei-yu frontal convergence. Category 2 primarily contains studies that quantitatively evaluate how BC signals feed the smaller-scale systems that directly induce the PHREs. For instance, Fu et al. (2016a,b) and Zhang et al. (2016) calculated the energy budgets of PHREs over the Yangtze River basin and found that a notable downscale kinetic energy (KE) cascade in the lower troposphere dominates the persistence of precipitation-related eddy flow. Within this category, two further scientific questions remain to be answered: (i) How do each of the BC signals interact with the smaller-scale systems that directly induce heavy precipitation during a PHRE, and (ii) how can we determine the relative importance of different BC signals in the scale interactions that sustain a PHRE? This study will address these two questions by applying a piecewise energy budget to a PHRE that occurred during the 2016 mei-yu season.

The remainder of this study is structured as follows: Section 2 describes the dataset and the piecewise energy budget method. Section 3 includes a general description of the PHRE and its main energy characteristics. Section 4 analyzes the interactions between various BC signals and precipitation-related eddy flow. Sensitivity experiments that seek to identify the relative importance of various BC signals are discussed in section 5. Finally, conclusions and a discussion are presented in section 6.

2. Data and methodology

a. The dataset

The National Centers for Environmental Prediction (NCEP) Climate Forecast System, version 2 (CFSv2), 6-hourly 0.5° × 0.5° products (Saha et al. 2014) were used in the analysis and energy budget calculations. This dataset was also used to generate the initial and boundary conditions for the semi-idealized experiments in this study. Rain gauge–based hourly accumulated precipitation data from the China Meteorological Administration were used to conduct wavelet analyses and to validate the results of the semi-idealized simulations.

b. The piecewise energy budget method

Based on the research of Fu et al. (2016a), energy budget equations based on temporal-scale separation (Murakami 2011) were used in this study. The equations used are as follows:

$$\partial A_M/\partial t = G(A_M) - C(A_M, K_M) - C(A_M, A_I) - B(A_M) + R(A_M), \quad (1)$$

$$\partial K_M/\partial t = C(A_M, K_M) - C(K_M, K_I) - D(K_M) - B(K_M), \quad (2)$$

$$\partial \overline{A_T}/\partial t = G(\overline{A_T}) - C(\overline{A_T}, \overline{K_T}) - C(\overline{A_T}, A_I) - B(\overline{A_T}), \quad (3)$$

$$\partial \overline{K_T}/\partial t = C(\overline{A_T}, \overline{K_T}) - C(\overline{K_T}, K_I) - D(\overline{K_T}) - B(\overline{K_T}), \quad (4)$$

where the overbar represents the temporal average, which can be regarded as the BC (Murakami 2011; Fu et al. 2016a), and the perturbation from this temporal average (which is denoted by a prime symbol in appendix A) is the eddy flow or smaller-scale system

that directly induces the heavy precipitation; A_M, K_M, A_T, and K_T are the available potential energy (APE) of the BC, the KE of the BC, the APE of the eddy flow, and the KE of the eddy flow, respectively. Terms $G(A_M)$ and $G(\overline{A_T})$ represent diabatic production/extinction of A_M and A_T, respectively. In this study, we only calculate precipitation-related diabatic processes, which are the most important diabatic effect for a PHRE (Fu et al. 2016a). In the calculation, the Kuo scheme (1974) is utilized, because it can reasonably capture the main characteristics of the diabatic processes associated with the mei-yu front (Zhao et al. 2004). Terms in the form of $C(X, Y)$ represent transfers between energies X and Y: a positive value means that energy is transferred from X to Y, while a negative value indicates a transfer of energy in the opposite direction. Boundary flux terms A_M, K_M, A_T, and K_T are represented by $B(A_M)$, $B(K_M)$, $B(\overline{A_T})$, and $B(\overline{K_T})$, respectively; $R(A_M)$ is the effect associated with vertical heat transport; and $D(K_M)$ and $D(\overline{K_T})$ denote the dissipation of K_M and K_T due to friction, respectively. Because the energy budgets are calculated using the CFSRv2 dataset, which is of a relatively coarser resolution, the budget terms may underestimate the intensity of the real energy conversion (Fu et al. 2016a,b). For more detailed descriptions of the physical significances and expressions of the budget terms, please refer to appendix A, Murakami (2011), and Fu et al. (2016a).

In this study, after confirming the importance of the eddy flow to the PHRE, we calculated the budget equations [Eqs. (1)–(4)] using a common methodology (i.e., a control calculation) to confirm whether the scale interactions are the dominant factors in determining the persistence of precipitation-related eddy flow. After this was confirmed, the BC was decomposed (by using the Lanczos bandpass filtering; Duchon 1979) into several components (i.e., a piecewise processing of the BC) according to the wavelet analysis (Erlebacher et al. 1996) of the BC. The typical BC signal was first removed from the original BC, resulting in a "minus" BC. It was then added to the original BC to form a "plus" BC. Both the minus and plus BCs were used to recalculate the budget equation. We determined the contribution of the typical BC signal by comparing the recalculated results to those of the control calculation.

3. Overview of the PHRE and its energy paths

The 2016 mei-yu season began at 0000 UTC 13 June 2016 and ended at 0000 UTC 7 July 2016. According to the mei-yu climatological features documented by the China Meteorological Administration (http://cmdp.ncc-cma.net), the 2016 season was typical. Heavy rainfall events appeared frequently over the Yangtze River basin during this mei-yu season, but only one of them could satisfy the PHRE criteria defined by Wang et al. (2014; footnote 1 in the introduction). This PHRE occurred from 0000 UTC 29 June to 0000 UTC 4 July 2016. It can be further divided into two precipitation periods with significantly different circulation configurations (not shown). The later period, which ranges from 0000 UTC 2 July to 0000 UTC 4 July 2016, is particularly noteworthy, because 1) the amount and intensity of precipitation (as Fig. 1a shows, the maximum precipitation accumulated over 48 h is more than 300 mm) significantly exceed those of the earlier period and 2) it caused severe flash flooding and urban waterlogging in the middle and lower reaches of the Yangtze River that resulted in huge economic losses. Therefore, in this study, the later precipitation period was considered using the piecewise energy budgets.

a. PHRE overview

The circulation configuration during the period from 0000 UTC 2 July through 0000 UTC 4 July 2016 is typical of a PHRE in the mei-yu season (Tao 1980; Zhao et al. 2004). As shown in Fig. 1b, two closed lows appear in the high latitudes. One is located north of Lake Balkhash and the other is located northeast of Lake Baikal. Between the two lows, a ridge maintains quasi-stationary behavior over Mongolia. The northwesterly wind ahead of the ridge line steers relatively cold, dry air from the higher latitudes to the lower latitudes. In the middle latitudes, the western Pacific subtropical high is strong and quasi stationary, west of which a 500-hPa shortwave trough maintains its intensity over central–eastern China. Behind the trough base, the northwesterly wind also contributes to a southward flow of relatively cold, dry air. Ahead of the trough base, favorable quasigeostrophic forces (i.e., warm temperature and cyclonic vorticity advection) that promote ascending motion (Holton 2004) appear over the precipitation region (i.e., the blue box in Fig. 1b). In addition, the precipitation region is located around the right entrance region of the upper-level jet, where the associated secondary circulation also contributes to the development of ascending motion (Holton 2004). A vigorous lower-level jet appears along the western periphery of the subtropical high. It continuously steers relatively warm, moist air from lower latitudes to the precipitation region, where it encounters the aforementioned cold, dry air. This situation favors persistent, heavy precipitation (Tao 1980; Ding 1993; Zhao et al. 2004; Bao 2007).

As the 850-hPa shear line and the 850-hPa potential pseudoequivalent temperature gradient show (Fig. 1c), the mei-yu front is mainly oriented in a southwest–northeast direction during the 48-h precipitation period. This orientation is the same as that of the accumulated precipitation (Fig. 1a). Because the mei-yu front is located primarily in the lower troposphere (Tao 1980;

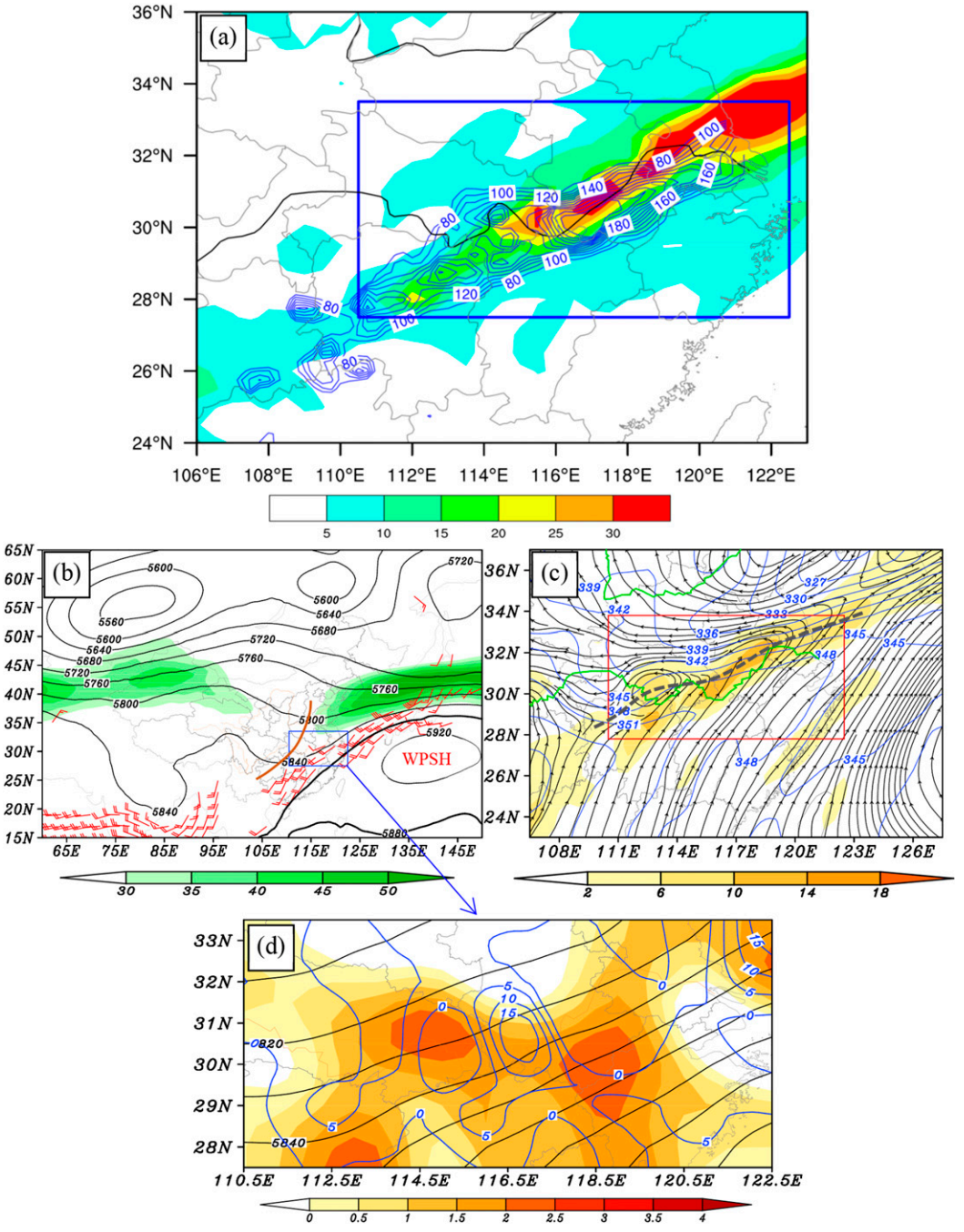

FIG. 1. (a) The 48-h accumulated precipitation (solid blue; mm) and the 48-h mean of the vertically averaged (from 900 to 700 hPa) K_T (shaded; J kg^{-1}). The blue box shows the target region. (b) The 48-h-averaged 500-hPa geopotential height (solid black; gpm), 200-hPa wind speed above 30 m s^{-1} (shaded; m s^{-1}), and 850-hPa wind field above 12 m s^{-1} (red wind barbs, with a full bar representing 8 m s^{-1}). The thick brown line is the trough line, the blue box is the target region, and WPSH is the western Pacific subtropical high. (c) The 48-h-averaged 850-hPa streamlines, relative vorticity (shaded; 10^{-5} s^{-1}), and potential pseudoequivalent temperature (solid blue; K). The thick gray line is the shear line, and the red box marks the target region. (d) An enlarged view of the target region, where the shading is the 48-h-averaged 500-hPa warm advection (10^{-5} K s^{-1}), the solid black is the 48-h-averaged 500-hPa geopotential height (gpm), and the blue solid is the 48-h-averaged 500-hPa vorticity advection (10^{-10} s^{-2}).

Zhao et al. 2004; Fu et al. 2016a), we calculate a lower-level vertical mean of K_T in the 950–700-hPa layer (950 hPa is used to avoid calculations below the topography) to reflect its energy features. A 48-h temporal average of this vertical mean is shaded in Fig. 1a. It is obvious that the mei-yu front–related K_T is consistent with the rainband. During the 48-h rainfall period, the eddy flow makes a mean contribution of ~70% (~65%) to the cyclonic vorticity (ascending motions) within the precipitation region (not shown). Based on the precipitation, mei-yu front–related K_T, lower-level shear line, and lower-level potential pseudoequivalent temperature gradient, a target region (27.5°–33.5°N, 110.5°–122.5°E; marked with boxes in Fig. 1) was selected for calculation of a horizontal mean that can represent the overall features within the precipitation region. Calculations based on this box are confirmed to be insensitive to relatively small changes in the box boundaries (each box boundary line ±1°; not shown), which guarantees that it is representative. The correlation coefficient between the target-region averaged hourly precipitation and the target-region averaged lower-level K_T is ~0.73, which exceeds the 95% confidence level. This means the precipitation variation is consistent with the mei-yu front–related K_T. Therefore, as discussed above, the mei-yu front–related eddy flow largely triggers the heavy precipitation (Zhao et al. 2004; Fu et al. 2016a).

b. *Energy paths of various layers*

Because the heavy precipitation lasted for 48 h (0000 UTC 2 July–0000 UTC 4 July 2016), we used 48 h as the time window for calculation of the temporal mean [as did Fu et al. (2016a)]. Thus, the BC for this study are the multiscale systems with periods longer than 48 h. Budgets were calculated using Eqs. (1)–(4), and a horizontal average was applied to the results within the target region (blue box in Fig. 1a) to focus on the heavy rainfall event. After that, the horizontal mean values were integrated vertically in three layers of equal mass (i.e., 950–700, 650–400, and 350–100 hPa) and the total layer (i.e., 950–100 hPa) as well. The results are used to represent the overall energy features in various layers of the precipitation region. Four energy paths were derived from the results of Eqs. (1)–(4), as shown in Fig. 2 (Fig. 2 is based on the energy budget results shown in Fig. B1 in appendix B).

Figure 2a shows that, within the total layer, downscale energy cascade (DSEC) processes that transfer energy from the BC to the eddy flow appear in both the APE and the KE. However, these energy cascade processes (i.e., interactions between BCs and eddy flows) do not dominate the BC or eddy flow variation. The APE of the BC is maintained primarily via net-import transport of A_M by the BC [i.e., $B(A_M)$], while the baroclinic energy conversion (BCEC) from the APE to the KE [i.e., $C(A_M, K_M)$] is its most important mechanism of consumption. The energy converted via the BCEC dominates the production of K_M, while the net-export transport of K_M by the BC [i.e., $B(K_M)$] is the factor most detrimental to sustaining K_M.

Precipitation-related diabatic processes [i.e., $G(\overline{A_T})$] dominate the production of eddy-flow APE, which is mainly consumed by the BCEC in the eddy flow [i.e., $C(\overline{A_T}, \overline{K_T})$]. Meanwhile, the BCEC dominates the production of K_T, while the net-export transport of K_T by both the BC and the eddy flow [i.e., $B(\overline{K_T})$] is the primary factor opposing increases in the former quantity. Overall, two energy paths that contribute to sustaining the eddy flow KE are presented via the thin gray lines in Fig. 2a.

In the upper troposphere, interactions between the BC and eddy flow are obvious. They can be reflected by an APE DSEC (Fig. 2b) and a KE upscale energy cascade (UPEC; i.e., KE is transferred from the eddy flow to the BC, which is the feedback effect of the eddy flow). The BC variation due to these two energy cascade processes can be neglected, but their effects on the eddy flow are important, because the energy transferred from K_T to K_M dominates the consumption of K_T. In contrast to the total layer, only one energy path that favors K_T enhancement appears in the upper layer (thin gray lines in Fig. 2b). This energy path is similar to that shown in the total layer (cf. Figs. 2a and 2b).

In the middle troposphere, a weak DSEC process appears in the KE (which can be neglected with regard to K_T variation), but no energy cascade occurs in the APE. This means that interactions between the BC and the eddy flow are weak. Precipitation-related diabatic processes are the primary source of A_T, which dominates the production of K_T via BCEC in the eddy flow. An energy path similar to that observed in the total layer (thin gray line in Fig. 2c) also contributes to the enhancement of K_T but is of secondary importance. Transport of K_T by both the BC and the eddy flow diverges primarily within the precipitation region and acts as the primary mechanism of K_T consumption.

The strongest KE and APE DSECs appear in the lower troposphere (Fig. 2d). This means that interactions between the BC and the eddy flow are intense. Although these DSEC processes are not important to variation of the BC, they dominate the production of A_T and K_T. One significant difference between the energy path in the lower layer and those in other layers is the presence of a weak BCEC that converts K_T to A_T. As reported by Fu et al. (2016a), the conversion direction of the BCEC is determined by activities of the warm air: active warm air tends to result in APE releases in the eddy flow (i.e., A_T is converted into K_T), while inactive

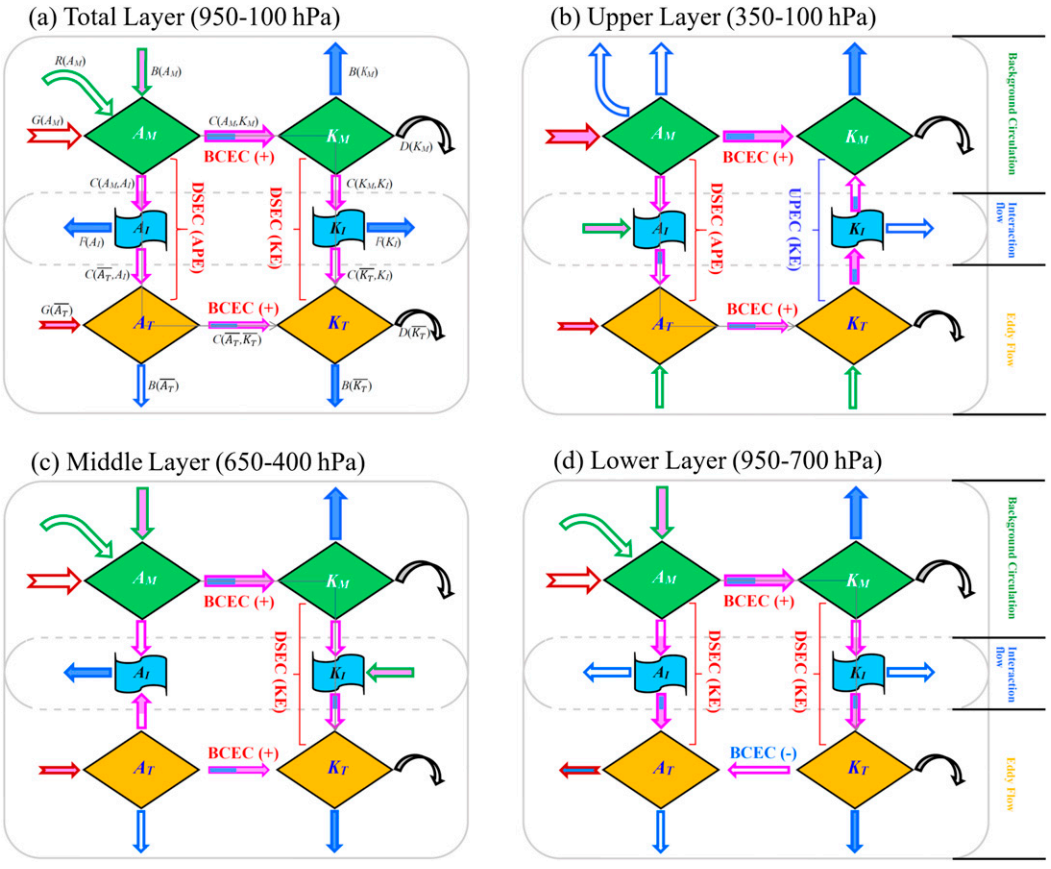

FIG. 2. The target-region averaged energy paths of various layers, where green arrows show net-import transport, blue arrows show net-export transport, purple arrows show conversions between different types of energies, dark red arrows show diabatic production/extinction of APE, curved arrows show the effects of dissipation terms, and the thin gray line with an arrow marks the energy path that enhances K_T. The dominant factor for the maintenance (dissipation) of each type of energy is shaded with light purple (blue). The purple arrows may be shaded in two colors because the conversions that they represent may be dominant factors for two types of energies. For BCEC, the plus and minus signs represent the release and production of APE, respectively.

warm air tends to cause conversion in the opposite direction. Overall, only one energy path contributes to enhancement of the mei-yu front–related K_T (thin gray line in Fig. 2d), which directly induces heavy precipitation. This energy path is similar to that of the total layer (cf. Figs. 2a and 2d).

4. Piecewise energy budget results

a. *BC decomposition*

As the direct trigger for the heavy precipitation event, the eddy flow interacts significantly with the BC (section 3). To understand how each BC signal interacts with the precipitation-related eddy flow, we compare the relative importance of various BC signals and identify those that are most important in these interactions. The comparisons are mainly based on the piecewise K_T energy budget [i.e., Eq. (4)] within the precipitation region.

The piecewise energy budget should be based on a reasonable BC decomposition. A wavelet analysis (Erlebacher et al. 1996) of the target-region averaged precipitation during the warm season of 2016 (from early April to late September) was conducted to identify the BC signals. From Fig. 3a, it is clear that the BC is composed of signals of various scales. Two wave crests appear in the global wavelet power spectrum (Fig. 3b) during the 48-h heavy precipitation period. However, only the stronger one (i.e., the QBO; 10–18 days) exceeds a 95% confidence level. The weaker longer-range oscillation (LRO; 40–128 days) exceeds only the 85% confidence level. This means that the QBO is the most significant BC signal in this 48-h heavy precipitation event. A wavelet analysis of the target-region averaged 850-hPa relative vorticity produces a similar result (not shown). For comparison, we added two other less significant BC signals to the BC decomposition: the

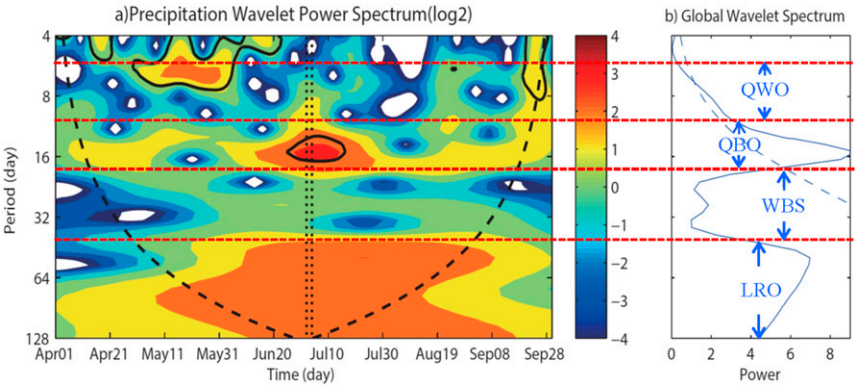

FIG. 3. Wavelet analysis of the target-region averaged precipitation using the Morlet wavelet. (a) The wavelet power spectrum (shaded), where solid black marks the 95% confidence level and the two vertical black dashed lines indicate the 48-h period of this heavy precipitation event. The thick long-dashed line indicates the cone of influence outside of which edge effects become important. (b) The 48-h-averaged wavelet power spectrum during this heavy precipitation event (solid dark blue) and the 95% confidence level (dark blue dashed line). Red dashed lines show the BC decomposition. QWO: 5–10 days; QBO: 10–18 days; WBS: 18–40 days; and LRO: 40–128 days.

quasi-weekly oscillation (QWO) with a period of 5–10 days and the weak BC signal (WBS), whose period is 18–40 days. In total, the periods of the QWO, QBO, WBS, and LRO range from 5 to 128 days and account for the dominant portion of the DSEC of KE (Table 1).

b. *Key factors in KE cascade processes*

As discussed in section 3b, a KE UPEC appears in the upper troposphere of the target region (Fig. 2b), while weak and strong KE DSECs occur in the middle and lower troposphere (Figs. 2c,d), respectively. A more detailed vertical distribution of the KE cascade processes (Fig. 4a) shows that the KE DSEC appears mostly below 525 hPa, while the KE UPEC occurs mostly above this level. In this study, we focus on the KE DSEC, which directly provides energy that sustains the precipitation-related eddy flow. To demonstrate the key features of the circulation configuration responsible for the KE DSEC, 800 hPa (it is near the central level of the mei-yu front, and it has a strong KE DSEC) was selected as the typical level for a detailed study.

A lower-level transversal trough with weak temperature gradients maintains quasi-stationary behavior over the target region during the 48-h precipitation period (Fig. 5a). As confirmed by several previous studies (Tao 1980; Zhao et al. 2004), the mei-yu front does not usually

TABLE 1. The mean and maximum rates of change (%) at levels below and above 525 hPa, respectively. A minus sign before the term in parentheses indicates filtering out, while a plus sign indicates summing. Abbreviations and durations are as follows: KMKI is $C(K_M, K_I)$; KTKI is $C(\overline{K_T}, K_I)$; QWO: 5–10 days; QBO: 10–18 days; WBS: 18–40 days; LRO: 40–128 days; and LP: 128 days.

	Below 525 hPa (DSEC of KE)		Above 525 hPa (UPEC of KE)	
	Average	Maximum	Average	Maximum
KMKI (−QWO)	−33.5	−59.6	−16.6	−64.8
KMKI (+QWO)	32.6	59.1	15.8	63.9
KTKI (−QWO)	−52.3	−156.5	−32.5	−65.7
KTKI (+QWO)	52.5	158.5	33.4	66.6
KMKI (−QBO)	−16.3	−21.9	−17.9	−35.5
KMKI (+QBO)	15.8	21.2	16.9	34.6
KTKI (−QBO)	−27.8	−95.1	−33.9	−53.2
KTKI (+QBO)	28.3	96.3	34.8	54.6
KMKI (−WBS)	−4.6	−10.1	−2.8	−9.1
KTKI (−WBS)	0.6	11.1	5.3	11.5
KMKI (−LRO)	−5.5	−13.9	−3.6	−14.9
KTKI (−LRO)	−2.3	−17.1	7.2	17.9
KMKI (LP)	−68.6	−109.3	−39.6	−170.3
KTKI (LP)	−83.7	−124.8	−56.8	−156.5

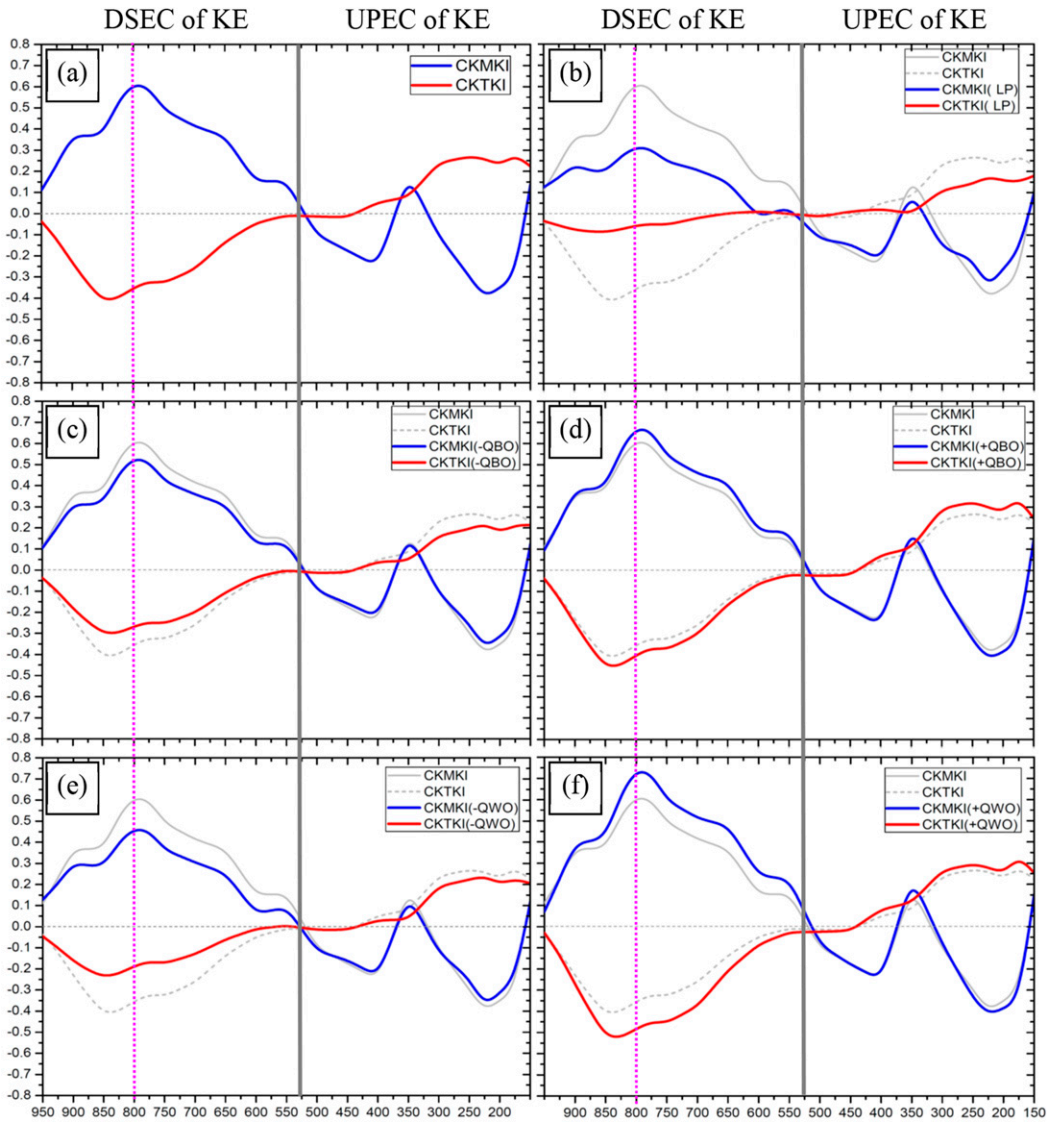

FIG. 4. Terms $C(K_M, K_I)$ (CKMKI; $10^{-3}\,\mathrm{W\,kg^{-1}}$) and $C(\overline{K_T}, K_I)$ (CKTKI; $10^{-3}\,\mathrm{W\,kg^{-1}}$) in various budgets: (a) the budget using the original BC, (b) the result using LP BC (signals with periods shorter than 128 days filtered out), (c) the result using a BC with the QBO signal filtered out, (d) the result using a BC with the QBO signal added, (e) the result using a BC with the QWO signal filtered out, and (f) the result using a BC with the QWO signal added.

exhibit obvious temperature gradients. Strong cyclonic vorticity occurs primarily south of the transversal trough, where a southwest–northeast-oriented lower-level jet appears. In contrast, the region north of the trough features weak cyclonic vorticity and a weak easterly wind. A strong positive $C(K_M, K_I)$ (i.e., energy is transferred from K_M to K_I) and an intense negative $C(\overline{K_T}, K_I)$ (i.e., energy is transferred from K_I to K_T) appear in the target region (Fig. 5b). The two energy conversions superpose onto each other (making the KE DSEC obvious) and stretch in a southwest–northeast direction, consistent with the mei-yu front.

Terms $C(\overline{K_T}, K_I)$ and $C(K_M, K_I)$ were decomposed to identify their respective dominant components. As shown in appendix A, each of the above terms has three components. However, according to our calculations, the third component of these two terms affects the results only a small amount (not shown). After neglecting the third component, only two components remain in each term: $\overline{u'\mathbf{u}'} \cdot \mathrm{grad}\overline{u}$ and $\overline{v'\mathbf{u}'} \cdot \mathrm{grad}\overline{v}$ for $C(\overline{K_T}, K_I)$ and $\overline{u}\mathrm{div}\overline{u'\mathbf{u}'}$ and $\overline{v}\mathrm{div}\overline{v'\mathbf{u}'}$ for $C(K_M, K_I)$. These components indicate that the Reynolds stress and the circulation features of the BC are vital to KE-related interactions (Fu et al. 2016a). As Figs. 6a and 6b show, $\overline{v'\mathbf{u}'} \cdot \mathrm{grad}\overline{v}$,

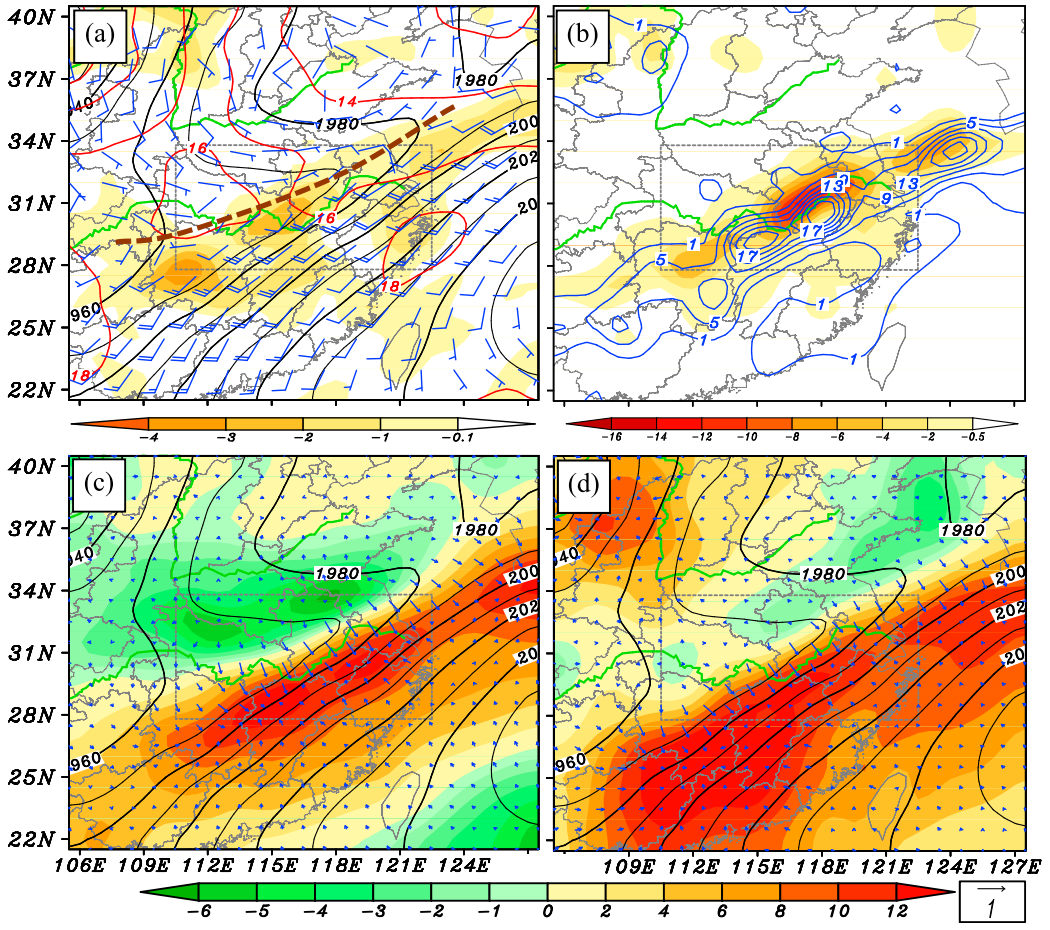

FIG. 5. (a) The 48-h-averaged 800-hPa geopotential height (solid black; gpm), wind field (full wind barb is 8 m s^{-1}), divergence (shaded; 10^{-5} s^{-1}), and temperature (solid red; °C). The brown dashed line shows the trough line of a transversal trough. (b) Terms $C(K_M, K_I)$ (solid blue; 10^{-4} W kg^{-1}) and $C(\overline{K_T}, K_I)$ (shaded; 10^{-4} W kg^{-1}) during the 48-h precipitation event. (c) The 48-h-averaged 800-hPa zonal wind (shaded; m s^{-1}), geopotential height (solid black; gpm), and zonal wind horizontal gradient (blue vectors; 10^{-4} s^{-1}). (d) The 48-h-averaged 800-hPa meridional wind (shaded; m s^{-1}), geopotential height (solid black; gpm), and horizontal gradient of meridional wind (blue vectors; 10^{-4} s^{-1}). The gray dashed boxes mark the target region.

which has the same distribution as $C(\overline{K_T}, K_I)$, is much stronger than $\overline{u'\mathbf{u}'} \cdot \text{grad}\overline{u}$. This means that $\overline{v'\mathbf{u}'} \cdot \text{grad}\overline{v}$ is the dominant factor in this term. The term $\overline{v'\mathbf{u}'} \cdot \text{grad}\overline{v}$ can be further decomposed into its zonal, meridional, and vertical components. The meridional component $\overline{v'v'}\,\partial\overline{v}/\partial y$ is the most important of these (Fig. 7a). As Fig. 5d shows, the strongest horizontal gradient of meridional wind within the target region mainly appears along the mei-yu front, where convergence occurs (i.e., $\partial\overline{v}/\partial y < 0$). Figure 8b shows that the strongest $\overline{v'\mathbf{u}'_h}$ also appears along the mei-yu front, and its meridional component is stronger than its zonal component (i.e., the transport of v' by the eddy flow is mainly in the meridional direction). The above configuration can explain why a strong negative $C(\overline{K_T}, K_I)$ appears along the mei-yu front. The physical significance and image of the conversion from K_I to K_T due to $\overline{v'v'}\,\partial\overline{v}/\partial y$ is shown in Fig. A1b of Fu et al. (2016a).

Similarly, for $C(K_M, K_I)$, we first compare $\overline{u}\text{div}\overline{u'\mathbf{u}'}$ and $\overline{v}\text{div}\overline{v'\mathbf{u}'}$ (Figs. 6c and 6d) and find that the latter term is more important. Then we decompose it into horizontal and vertical components. A comparison of these two components shows that the horizontal component $\overline{v}\text{div}\overline{v'\mathbf{u}'_h}$ is the dominant factor in $C(K_M, K_I)$ (Fig. 7b). From Figs. 5d and 8b, it can be seen that convergence of $\overline{v'\mathbf{u}'_h}$ (i.e., $\text{div}\overline{v'\mathbf{u}'_h} < 0$) occurs primarily north of the lower-level transversal trough (Fig. 8b), where the northerly wind (i.e., $\overline{v} < 0$) is dominant (Fig. 5d). In contrast, divergence of $\overline{v'\mathbf{u}'_h}$ (i.e., $\text{div}\overline{v'\mathbf{u}'_h} > 0$) appears primarily south of the transversal trough (Fig. 8b), where the southerly wind (i.e., $\overline{v} > 0$) is dominant (Fig. 5d). Both of these configurations result in

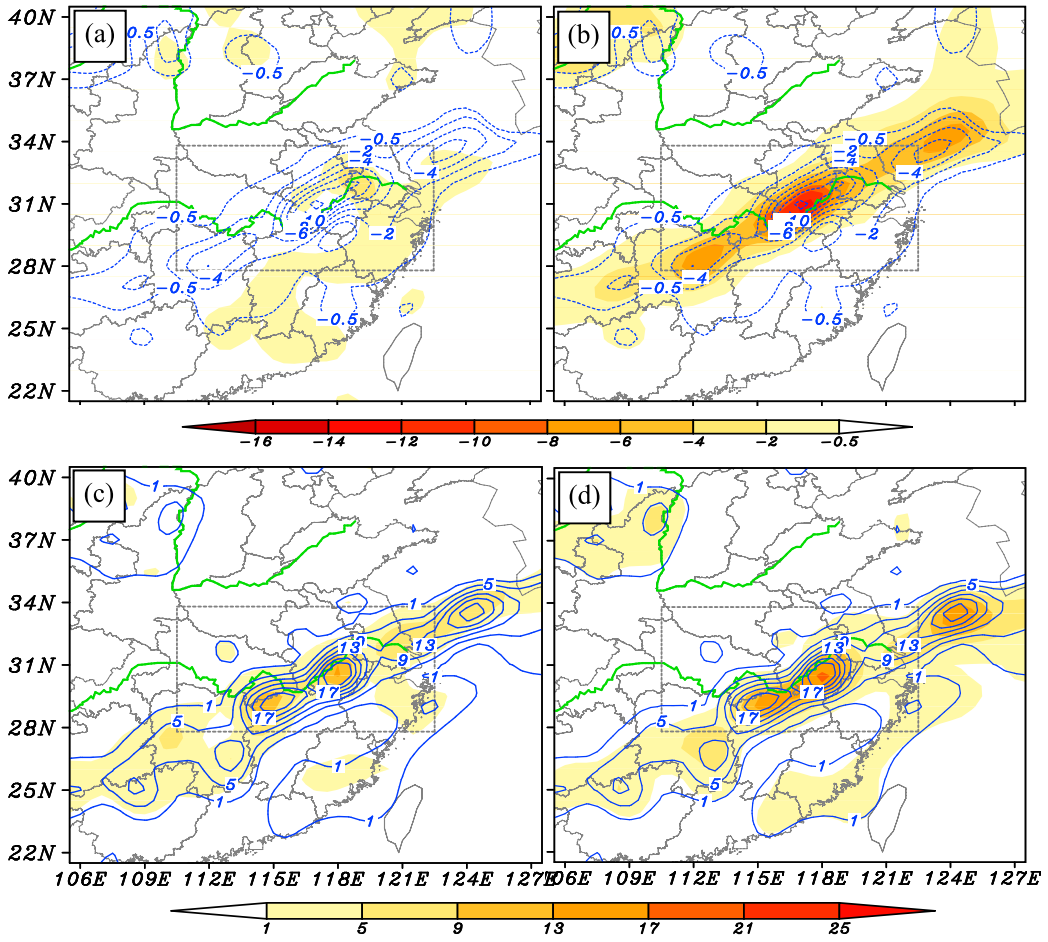

FIG. 6. (a),(b) The $\overline{u'\mathbf{u}'} \cdot \mathrm{grad}\overline{u}$ and $\overline{v'\mathbf{u}'} \cdot \mathrm{grad}\overline{v}$ components of $C(\overline{K_T}, K_I)$ (shaded; $10^{-4}\,\mathrm{W\,kg^{-1}}$), respectively. The blue dashed lines show $C(\overline{K_T}, K_I)$ ($10^{-4}\,\mathrm{W\,kg^{-1}}$), and the gray dashed box indicates the target region. (c),(d) The $\overline{u}\mathrm{div}\overline{u'\mathbf{u}'}$ and $\overline{v}\mathrm{div}\overline{v'\mathbf{u}'}$ components of $C(K_M, K_I)$ (shaded; $10^{-4}\,\mathrm{W\,kg^{-1}}$), respectively. The blue dashed lines show $C(K_M, K_I)$ ($10^{-4}\,\mathrm{W\,kg^{-1}}$), and the gray dashed box indicates the target region.

positive $\overline{v}\mathrm{div}\overline{v'\mathbf{u}'_h}$ values (i.e., energy is transferred from K_M to K_I), which is orientated along the mei-yu front. Details of the physical significance and an image of this conversion are discussed in section B1.1 of Fu et al. (2016a).

c. *Piecewise KE cascade energy budget*

1) LOW-PASS BC RESULTS

A budget analysis of the eddy flow within the target region based on Eq. (4) was conducted (section 3b). Results show that, for levels below 525 hPa, the KE of the eddy flow is primarily maintained via terms $C(\overline{K_T}, K_I)$ (i.e., the DSEC of the KE) and $C(\overline{A_T}, \overline{K_T})$ (i.e., the BCEC of the eddy flow), while terms $B(\overline{K_T})$ and $D(\overline{K_T})$ act in the opposite manner (not shown). The term $C(\overline{K_T}, K_I)$ is the most favorable factor and accounts for ~75% of the total energy converted into K_T. This means that interactions between the BC and the eddy flow are crucial to the persistence of the precipitation-related eddy flow during this event.

In this study, the time window used to calculate Eqs. (1)–(4) is 48 h. The total flow was decomposed into the eddy flow (with periods ≤48 h) and the BC (with periods >48 h; Fu et al. 2016a). Because we used the warm season of 2016 (from early April to late September) to analyze the BC signals, the maximum period that could be properly identified via wavelet analysis was ~128 days (Fig. 3). A Lanczos filter (Duchon 1979) was used to obtain a 128-day low-pass (LP) BC using an extended time series that considers the period from early March to late October. That is, only signals with periods >128 days are retained in the BC. Equation (4) is recalculated using this modified BC, while the eddy flow is the same as that used in section 3b. The result is shown in Fig. 4b. Term

$C(\overline{K_T}, K_I)$, which references interactions between the eddy and interaction flows, weakens in the total air column. In contrast, $C(K_M, K_I)$ (i.e., interactions between the BC and the interaction flow) only weakens substantially below 525 hPa (Fig. 4b), while the changes are moderate above 525 hPa. To quantify the change that occurs after modifying the BC, a changing rate was defined as

$$\text{Changing rate of term } S = \frac{\text{Term } S \text{ (using the modified BC)} - \text{Term } S \text{ (using the original BC)}}{\text{Term } S \text{ (using the original BC)}}.^{2}$$

This rate was calculated at 25-hPa intervals from 950 to 150 hPa. The changing rates at 950–525 and 525–150 hPa were averaged to determine the overall/mean changes in the corresponding layers and are shown in Table 1. Filtering out BC signals with periods shorter than 128 days reduces the intensities of $C(\overline{K_T}, K_I)$ and $C(K_M, K_I)$, particularly below 525 hPa, where the mean rate of decrease is more than 68%. At levels below 525 hPa, BC signals with periods of less than 128 days dominate the KE DSEC within the target region. In contrast, at levels above 525 hPa, a 39.6% mean rate of decrease appears in the term $C(K_M, K_I)$ (Table 1). Thus, the feedback on the BC through the KE UPEC in this layer is more closely related to BC signals with periods of more than 128 days than to signals with shorter periods. The KE UPEC will be investigated in detail in a future work.

2) Importance of the QBO and QWO signals

We evaluate the importance of the QBO signal first because it is the most significant BC signal in this study. The QBO signal was determined via Lanczos bandpass filtering (Duchon 1979) of the time series from early March to late October. Equation (4) was recalculated after filtering out or summing the QBO signals in the BC. Because the calculations use the same eddy flow, the difference in the BC is the only reason for changes in $C(\overline{K_T}, K_I)$ and $C(K_M, K_I)$. The results are shown in Figs. 4c and 4d, from which it is clear that the QBO signal favors a KE cascade in the total air column. Below 525 hPa, the mean rate of change of the KE DSEC due to the QBO signal is typically between 15% and 29% (Table 1). Overall, the conversion between eddy and interaction flows [i.e., $C(\overline{K_T}, K_I)$] exhibits more dependence on the QBO signal than the conversion between the BC and the interaction flow [i.e., $C(K_M, K_I)$] (Table 1). One possible reason for this phenomenon is explained below (using 800 hPa as an example).

From section 4b, $\overline{v'v'}\,\partial\overline{v}/\partial y$ and $\overline{v}\mathrm{div}\overline{\mathbf{v}'\mathbf{u}'_h}$ are the controlling factors for $C(\overline{K_T}, K_I)$ and (K_M, K_I) at 800 hPa, respectively. The 48-h-averaged 800-hPa QBO bandpass-filtering results are shown in Figs. 9a and 9c. The QBO signal features a southwest–northeast-oriented weak low pressure/height belt within the target region. This belt is associated with a southwest–northeast-oriented weak shear line, a weak convergence zone, and a weak temperature gradient (Fig. 9a). Filtering out (summing) the QBO signal in the BC is equivalent to weakening (enhancing) the lower-level transversal trough, shear line, and corresponding convergence (Fig. 5a), which affects the KE DSEC below 525 hPa. A bilaterally symmetric structure along the diagonal of the target region appears in the meridional wind field (Fig. 9c), and the meridional wind south of the diagonal is stronger than that north of the diagonal. Thus, when considering the mean of the target region, the negative (north of the diagonal) and positive meridional (south of the diagonal) winds cancel each other out, producing only a weak positive $\overline{v}$. In contrast, the target-region averaged $\partial\overline{v}/\partial y$ changes more significantly, because the above configuration corresponds primarily to convergence in the target region (Fig. 9c) and no obvious offset is present. Thus, $\overline{v'v'}\,\partial\overline{v}/\partial y$ is more sensitive to the QBO signal than $\overline{v}\mathrm{div}\overline{\mathbf{v}'\mathbf{u}'_h}$, which explains why $C(\overline{K_T}, K_I)$ changes more than $C(K_M, K_I)$ after filtering out or summing the QBO signals in the BC.

For comparison, the QWO signal was determined and calculated using Eq. (4) in a manner similar to that of the QBO signal. From Figs. 4e and 4f, the QWO signal also acts primarily to favor the KE cascade in the total air column. However, unlike the QBO signal, which offers similar contributions below and above 525 hPa (Table 1), the QWO signal offers a much larger contribution to the KE DSEC below 525 hPa. As Figs. 4e and 4f show, the KE DSEC exhibits remarkable responses to the QBO signal in the BC below 525 hPa. The mean changing rates of $C(K_M, K_I)$ and $C(\overline{K_T}, K_I)$ due to the QWO signal are approximately double those due to the QBO signal (Table 1). Thus, the QWO signal is significantly more important to the persistence of the precipitation-related eddy flow below 525 hPa.

[2] A positive changing rate means that modifying the BC enhances the intensity of term S (which is a sample term); a negative changing rate with an absolute value of less than 100% means that modifying the BC reduces the intensity of term S; and a negative changing rate with an absolute value of over 100% means that modifying the BC changes the sign of term S.

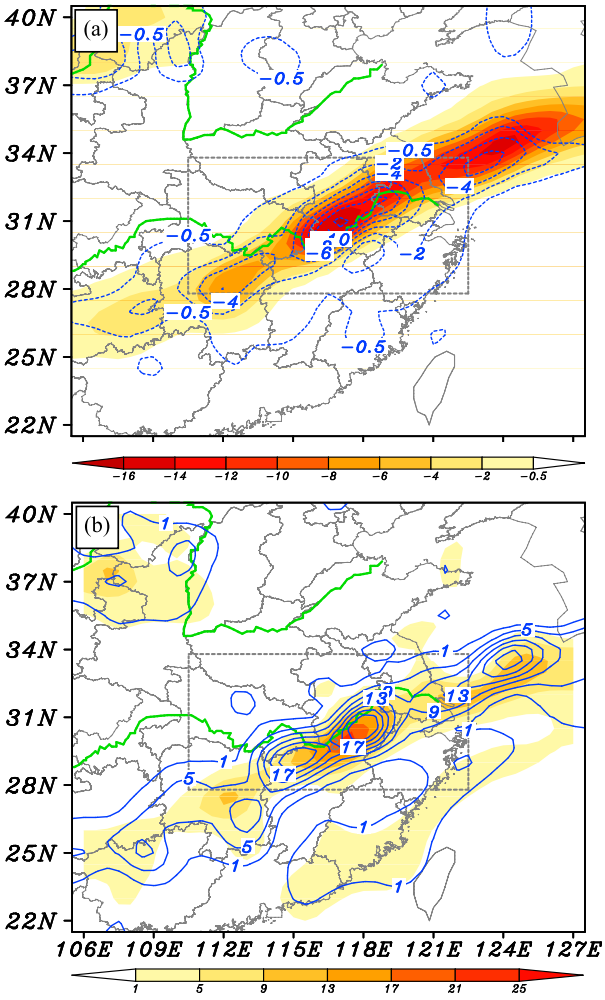

FIG. 7. (a) Plot of $\overline{v'v'}\partial\overline{v}/\partial y$ (shaded; 10^{-4} W kg^{-1}), which is the dominant factor for $C(\overline{K_T}, K_I)$. The blue dashed lines show $C(\overline{K_T}, K_I)$ (10^{-4} W kg^{-1}), and the gray dashed box shows the target region. (b) Plot of $\overline{v}\text{div}\overline{v'\mathbf{u}'_h}$ (shaded; 10^{-4} W kg^{-1}), which is the dominant factors for $C(K_M, K_I)$. The blue dashed lines show $C(K_M, K_I)$ (10^{-4} W kg^{-1}), and the gray dashed box indicates the target region.

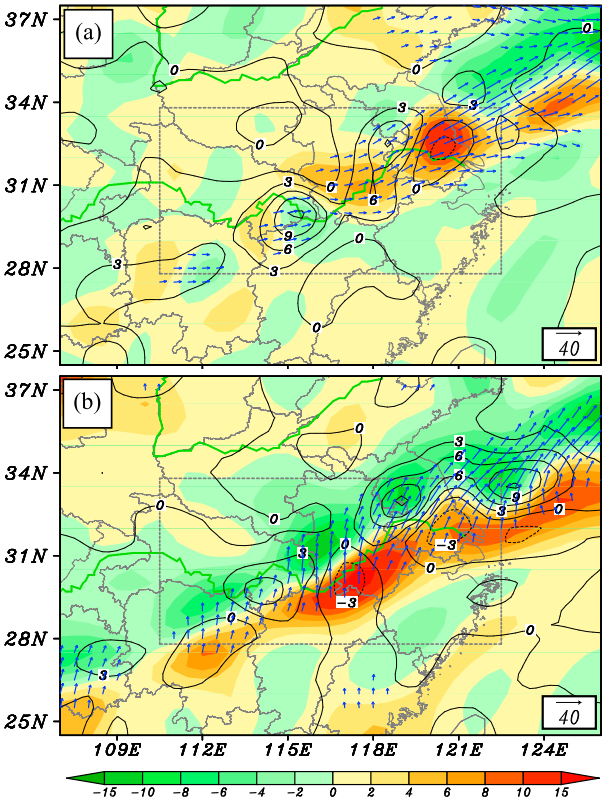

FIG. 8. (a) Plot of $\overline{u'\mathbf{u}'_h}$ above 10 m^2 s^{-2} (blue vectors), div$\overline{u'\mathbf{u}'_h}$ (shaded; 10^{-5} m s^{-2}), and div$\overline{u'\mathbf{u}'_v}$ (solid black; 10^{-5} m s^{-2}) during the 48-h precipitation period. (b) Plot of $\overline{v'\mathbf{u}'_h}$ above 10 m^2 s^{-2} (blue vectors), div$\overline{v'\mathbf{u}'_h}$ (shaded; 10^{-5} m s^{-2}), and div$\overline{v'\mathbf{u}'_v}$ (solid black; 10^{-5} m s^{-2}) during the 48-h precipitation period. The subscripts h and v indicate the horizontal and vertical components, respectively. The gray dashed boxes mark the target region.

As Fig. 9b shows, within the target region, the QWO signal also features a southwest–northeast-oriented weak low pressure/height belt that is associated with a shear line and convergent zone in the same orientation. The configuration is similar to that of the QBO signal but is more intense (see Figs. 9c and 9d). This may explain why the QWO signal also contributes to the KE DSEC below 525 hPa but in a more intense manner. Unlike the relative importance of the QBO and QWO in contributing to the KE DSEC below 525 hPa, the QBO signal is slightly more important to the KE UPEC than the QWO signal for levels above 525 hPa (Table 1).

3) IMPORTANCE OF THE LRO AND WBS SIGNALS

As Fig. 3 shows, the LRO is the second most significant BC signal in this study. As with the QBO signal, Lanczos bandpass filtering was applied to the time series from early March to late October. Then, the LRO signal was filtered from the BC, and Eq. (4) was recalculated using the remainder. Table 1 shows that the LRO signal is not important to the KE cascade (less than 6% below and less than 8% above 525 hPa). This is because the wind and geopotential height field associated with the LRO signal are much weaker than those associated with the QBO/QWO signals and are in a different configuration (not shown). Overall, the LRO signal contributes to the KE DSEC below 525 hPa (Table 1). At levels above 525 hPa, it favors transfers from K_I to K_M but disfavors transfers from K_T to K_I. This reduces the feedback effect from eddy flow within the precipitation region to the BC.

For comparison, the WBS signal was processed in the same manner as the LRO signal. As Table 1 shows, the WBS signal contribution is smaller than those of the other three BC signals. It is less than 5% (6%) at levels below (above) 525 hPa. Thus, the effect of the WBS signal

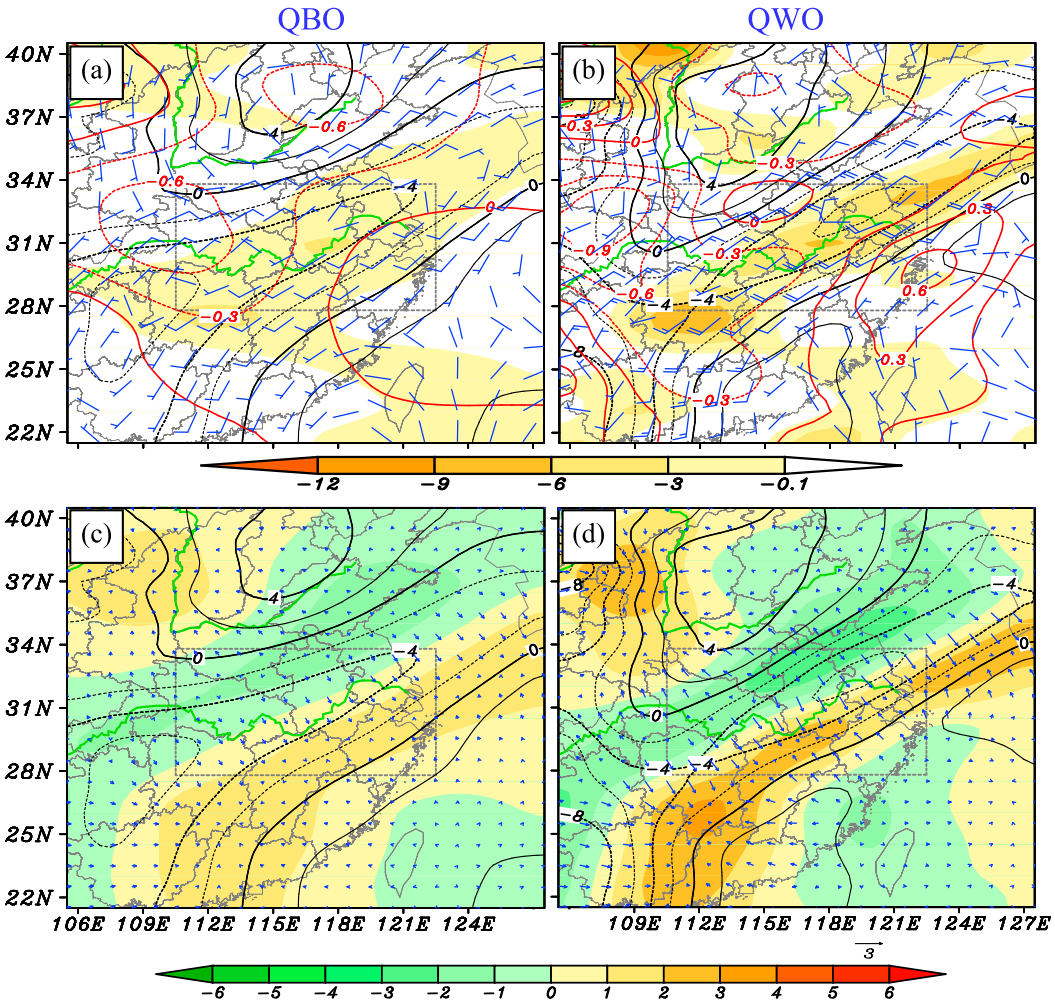

FIG. 9. (top) The 48-h-averaged (a) QBO and (b) QWO bandpass-filtered 800-hPa geopotential height (solid black; gpm), wind field (full wind barb is 2 m s^{-1}), divergence (shaded; 10^{-6} s^{-1}), and temperature (solid red; °C). (bottom) The 48-h-averaged (c) QBO and (d) QWO bandpass-filtered 800-hPa meridional wind (shaded; m s^{-1}), geopotential height (solid black; gpm), and the horizontal gradient of meridional wind (blue vector; 10^{-5} s^{-1}). The gray dashed boxes mark the target region.

on the KE cascade is negligible. The low intensities of the wind and geopotential height fields associated with the WBS signal (not shown) are possible reasons for the small size of its contribution. In the total air column, the WBS signal enhances the interaction between the BC and the interaction flow [i.e., $C(K_M, K_I)$] while slightly weakening the interaction between the eddy flow and the interaction flow [i.e., $C(\overline{K_T}, K_I)$]. Thus, the WBS signal slightly reduces the role of the eddy flow in the KE cascade.

5. Results of semi-idealized simulations

a. Model configuration

Although the QBO signal is the most significant BC signal in this study (Fig. 3), the QWO signal is the most important contributor to the maintenance of precipitation-related eddy flow below 525 hPa (Table 2). Three simulations were conducted to further confirm this: the original run (ORI), a run with QWO removed, and a run with QBO removed. All three simulations were conducted using a one-way, double-nested (15 and 3 km; d01 has 361 × 271 grid points and d02 has 901 × 721 grid points; Fig. 10), convection-permitting version of the Advanced Research version of WRF (Skamarock et al. 2008). The Noah (Chen and Dudhia 2001), the WRF single-moment 6-class microphysics scheme (WSM6; Hong and Lim 2006), and the Yonsei University (YSU) planetary boundary layer scheme (Noh et al. 2001) were used in both domains. The Kain–Fritsch cumulus parameterization (Kain 2004) was used in d01, while no cumulus parameterization was used in d02. CFSv2 data (0.5° × 0.5°; Saha et al. 2014) were used to generate initial and boundary conditions. All three runs were initiated at

TABLE 2. The contributions of various BC signals to KE cascade processes. Abbreviations are as follows: KMKI is $C(K_M, K_I)$, KTKI is $C(\overline{K_T}, K_I)$, F is favorable, and U is unfavorable. The numbers in parentheses show the relative intensities of different BC signals within a column, with a larger number indicating a larger contribution. Boldface indicates that BC signals dominate the energy cascade process.

	Below 525 hPa (DSEC of KE)		Above 525 hPa (UPEC of KE)	
	KMKI	KTKI	KMKI	KTKI
QWO	F (4)	**F (4)**	F (3)	F (3)
QBO	F (3)	F (3)	F (4)	F (4)
WBS	F (1)	U (1)	F (1)	U (1)
LRO	F (2)	F (2)	F (2)	U (2)

1200 UTC 1 July 2016 and set to run for 60 h in order to include the entire heavy precipitation event.

Lanczos bandpass filtering was used to remove the QWO/QBO signals from the target regions (purple box in Fig. 10) of d01 and d02 (using the time series from early March to late October). To reduce the imbalance between the target region and the remainder of the model domain caused by bandpass filtering, a relaxation zone that enlarges each boundary of the target region by 2.5° (the dashed white box in Fig. 10) was used. Within the relaxation zone, the QWO/QBO signal decreases linearly to zero as it approaches the target region.

b. *Simulation results*

The ORI simulation reproduced the main circulation features shown by the CFSv2 data well. This includes the upper-level jet, 500-hPa short-wave trough, western Pacific subtropical high, and lower-level transversal trough (not shown). Comparisons of Figs. 1b,c and Fig. 11a show that the lower-level jet and the 850-hPa southwest–northeast-oriented shear line have been reproduced reasonably. Comparisons of Figs. 1a and 12a show that the ORI simulation reproduces the southwest–northeast-oriented rain belt well within the target region. Although there are differences between simulated and observed precipitation (e.g., the precipitation center around 30°N, 117°E is underestimated, while the precipitation center around 29°N, 115°E is overestimated), the intensity of the precipitation is reproduced reasonably. As discussed above, the ORI simulation reproduces the salient features of the precipitation event that occurred between 0000 UTC 2 July and 0000 UTC 4 July 2016 and thus can be used for further analyses.

Comparing Figs. 12a–e shows that removal of the QWO/QBO signals from the BC causes a decrease in the 48-h accumulated precipitation. This confirms the piecewise energy budget results from these two BC

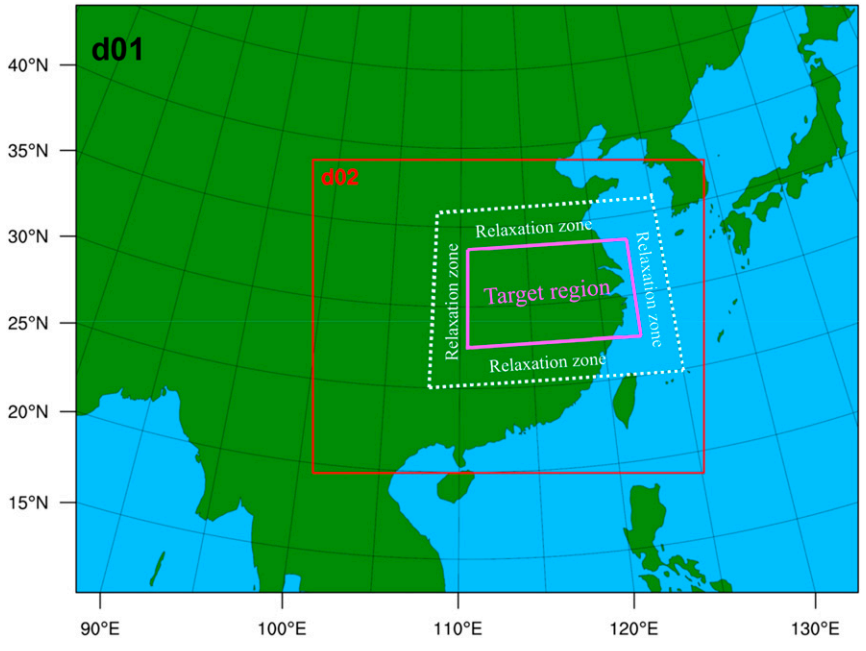

FIG. 10. The two domains used for simulation, where the solid purple line marks the target region and the white dashed line shows a relaxation zone (enlarged by 2.5° to each boundary line of the target zone).

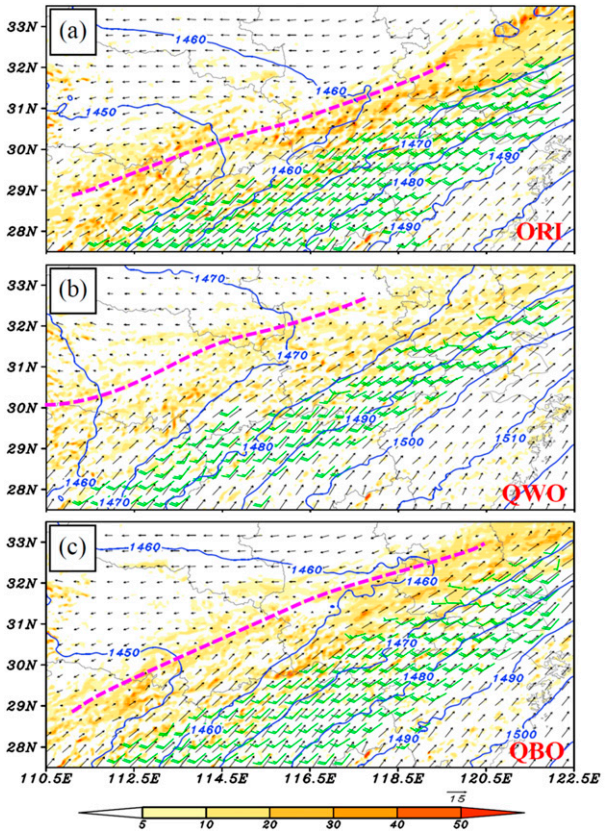

FIG. 11. The 48-h-averaged 850-hPa geopotential height (solid blue; gpm), wind (black arrows; m s^{-1}), vorticity (shaded; 10^{-5} s^{-1}), and wind with speeds that exceed 12 m s^{-1} (green wind bars, with a full bar representing 8 m s^{-1}) in (a) the ORI , (b) the QWO , and (c) the QBO runs, where the thick purple dashed lines are the transversal trough.

signals; that is, the QWO/QBO signals favor the precipitation event (Table 2). Further comparison of Figs. 12b–e shows that removing the QWO signal from the BC results in a more obvious precipitation reduction than removing the QBO signal. This is also consistent with the piecewise energy budget results; that is, the QWO signal is more important than the QBO signal during this event. As Fig. 11 shows, removing the QWO/QBO signals causes an obvious reduction of the lower-level shear line and transversal trough intensities, thus weakening the precipitation-related eddy flow. Thus, the precipitation weakens as well. This is consistent with the discussion in section 4c, which is based on Fig. 9. Comparison of Figs. 11b and 11c shows that the lower-level shear line and transversal trough weaken more significantly in the simulation in which QWO is removed. In addition, the lower-level jet exhibits a larger intensity decrease due to QWO signal removal. Therefore, the precipitation-related eddy flow is weakened more significantly in the simulation with QWO removed, resulting in a larger precipitation reduction.

6. Conclusions and discussion

A PHRE is a product of the combined effects of multiscale systems. Clarifying the interactions between the precipitation-related smaller-scale systems and the larger-scale BC is a useful way of understanding PHREs. This may provide a basis for medium- to long-range PHRE forecasting. If the numerical model can forecast the dominant BC signals credibly (e.g., the QWO signal in this study) and we can determine the regions where these BC signals persistently transfer energy to smaller-scale systems (based on studies similar to this one), a PHRE can be forecast on a mid- to long-term temporal scale. This ensures sufficient time to cope with the related disasters. For this purpose, it is important to understand how each dominant BC signal interacts with the smaller-scale precipitation-related systems and to determine their relative importance. This study focuses on these goals by conducting a piecewise energy budget analysis of a typical PHRE, which occurred in the 2016 mei-yu season.

The upper-, mid-, and lower-tropospheric energy paths of this PHRE were derived (Fig. 2) based on the budget results using Eqs. (1)–(4). Overall, interactions between the precipitation-related eddy flow and its BC occur at all levels. The strongest interactions occur in the lower troposphere (the mei-yu front is located primarily in this layer), which is characterized by a significant KE DSEC and an APE DSEC. The KE DSEC is the unique dominant factor that contributes to the persistence of the precipitation-related eddy flow in this event. This means that the scale interaction is crucial to the occurrence of this PHRE. The significant KE DSEC in the lower troposphere was also found in 10 other PHREs documented by Fu et al. (2016a) and Zhang et al. (2016). It seems that this is an important common feature of the PHREs. The weakest interaction associated with this PHRE appears in the middle troposphere, where only a weak KE DSEC occurs. The UPEC (i.e., the feedback from the eddy flow on the BC) is also significant, particularly at levels above 525 hPa, but its effect on BC variation is negligible. This means that a single PHRE cannot change the status of its large-scale BC. Fu et al. (2016a) and Zhang et al. (2016) drew the same conclusion in their studies.

Usually, the typical BC signals are identified by conducting a wavelet/power-spectrum analysis (Mao and Wu 2006; Li et al. 2014; Liu et al. 2014). In this study, the wavelet analysis was applied to the precipitation and vorticity field, both of which confirm that the QBO signal is the most significant BC signal. Traditionally, the QBO signal is expected to be the most important scale interaction factor during the PHRE. This is true for the KE UPEC at levels above 525 hPa, where the QBO accounts for the largest percentage among the four BC signals (Table 2). However, at levels below 525 hPa, the

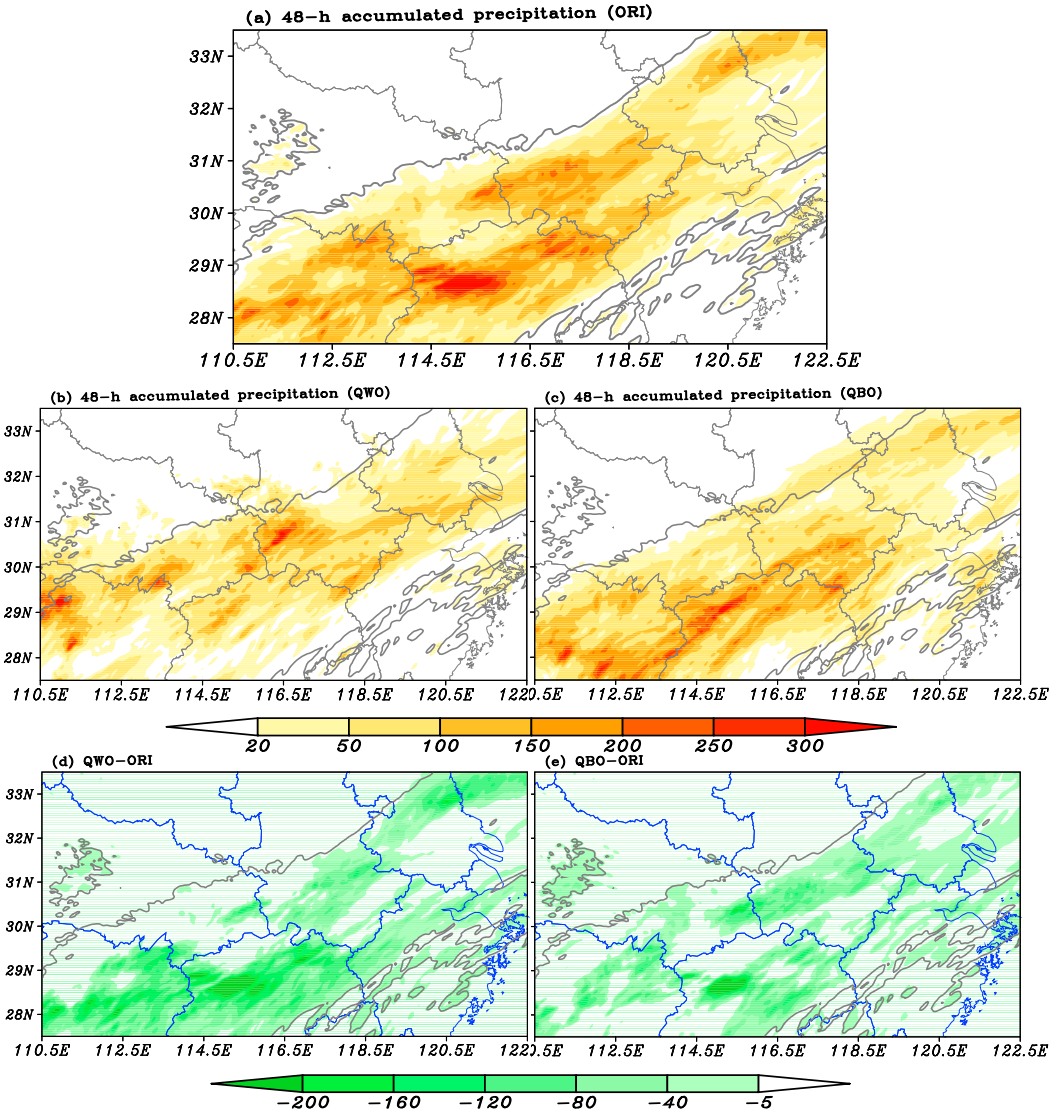

FIG. 12. The 48-h accumulated precipitation (shaded; mm) for (a) the ORI, (b) the QWO run with the QWO signal filtered out, and (c) the QBO run with the QBO signal filtered out. (d) The difference (shaded; mm) between the 48-h accumulated precipitation in the QWO and ORI runs. (e) As in (d), but for the difference between the QBO and ORI runs. The thick gray line is the 10-mm isoline in the ORI run.

QBO signal does not play the leading role in the KE DSEC that directly sustains the precipitation-related eddy flow. The LRO is the second most significant BC signal but is not important to the KE DSEC in this layer either. Instead, the QWO is the most important BC signal affecting the KE DSEC below 525 hPa. Semi-idealized simulations of the QBO/QWO signals also confirm that the precipitation and intensities of the lower-level shear line and transversal trough are more dependent on the QWO signal. Thus, for a PHRE, the relative importance of different BC signals in the scale interactions cannot be determined using only a wavelet/power-spectrum analysis.

In this PHRE, the transition from a KE DSEC to a KE UPEC appears around 525 hPa. A KE DSEC appears below 525 hPa, while above this level, a KE UPEC occurs. Below 525 hPa, the KE DSEC shows more dependence on the BC signals with periods below 128 days. Comparisons of various BC signals show that those with shorter periods tend to have larger contributions (provide more energy) to the KE DSEC (Table 2). In this event, the QWO signal contributed the most to the KE DSEC. In contrast, at levels above 525 hPa, the KE UPEC exhibits more dependence on the BC signals with periods above 128 days. Thus, in this PHRE, the eddy flow feedback effect tends to transfer more energy to BC

signals with longer periods. Among the four BC signals we compared (Table 2), the QBO signal showed the largest contribution to the KE UPEC, but in the BC signals with periods above 128 days, there may be some more important factors. In summary, the BC components that govern KE cascades in the mid- to lower and mid- to upper troposphere are asymmetric.

Acknowledgments. The authors thank the National Centers for Environmental Prediction (NCEP) and the China Meteorological Administration for providing the data. This research was supported by the National Natural Science Foundation of China under Grants 41775046 (Shen-Ming Fu), 91637211(Xiao-Feng Xu), and 41405007 (Wan-Li Li)] and by the State Key Laboratory of Severe Weather, Chinese Academy of Meteorological Sciences under Grant 2016LASW-B05 (Jian-Hua Sun).

APPENDIX A

Definitions of Energies and Budget Terms

According to Murakami (2011), the definitions of various types of energies and energy budget terms are as follows:

$$A_M = \frac{C_p}{2}\left(\frac{p}{p_0}\right)^{2\kappa}\gamma(\overline{\theta}-\langle\overline{\theta}\rangle)^2,$$

$$A_T = \frac{C_p}{2}\left(\frac{p}{p_0}\right)^{2\kappa}\gamma\theta'^2, \quad \text{and}$$

$$A_I = C_p\left(\frac{p}{p_0}\right)^{2\kappa}\gamma\theta'(\overline{\theta}-\langle\overline{\theta}\rangle)$$

are the APE of the BC, eddy flow, and interaction flow, respectively, where the overbar represents the temporal average (i.e., the BC), the prime stands for the perturbation from this temporal average (i.e., the eddy flow), C_p is the atmospheric specific heat at constant pressure, p is the pressure, p_0 is the reference pressure, κ is the ratio of the gas constant to the specific heat, γ is the static stability index, θ is the potential temperature, and angle brackets represent the global-average operator. The sum of A_M, A_T, and A_I is the total APE. The KE of the BC, eddy flow, and interaction flow is

$$K_M = \frac{1}{2}(\overline{u}^2+\overline{v}^2),$$

$$K_T = \frac{1}{2}(u'^2+v'^2), \quad \text{and}$$

$$K_I = (\overline{u}u'+\overline{v}v'),$$

respectively. In these expressions, $\mathbf{u}=(u, v, \omega)$ is the three-dimensional wind field in the pressure coordinates. The sum of K_M, K_T, and K_I is the total KE. The diabatic generation/extinction of A_M is

$$G(A_M) = \gamma(\overline{T}-\langle\overline{T}\rangle)(\overline{Q}-\langle\overline{Q}\rangle),$$

where T is the temperature and Q is the diabatic heating/cooling rate. The baroclinic energy conversion of the BC is

$$C(A_M, K_M) = -\overline{\omega}\,\overline{\alpha},$$

where α is the specific volume. The conversion between A_M and A_I is

$$C(A_M, A_I) = C_p\left(\frac{p}{p_0}\right)^{2\kappa}\gamma(\overline{\theta}-\langle\overline{\theta}\rangle)\mathrm{div}\overline{\theta'\mathbf{u}'},$$

where div(·) is the divergence operator. The three-dimensional transport of A_M and other related factors by the BC is represented by

$$B(A_M) = C_p\left(\frac{p}{p_0}\right)^{2\kappa}\gamma\mathrm{div}\left[\frac{(\overline{\theta}-\langle\overline{\theta}\rangle)^2-\langle\overline{\theta}\rangle^2}{2}\overline{\mathbf{u}}\right].$$

The effect associated with vertical heat transport by both the BC and eddy flow is

$$R(A_M) = C_p\left(\frac{p}{p_0}\right)^{2\kappa}\gamma(\overline{\theta}-\langle\overline{\theta}\rangle)\left(\frac{\partial\langle\overline{\omega}\,\overline{\theta}\rangle}{\partial p}+\frac{\partial\langle\overline{\omega'\theta'}\rangle}{\partial p}\right).$$

The conversion between K_M and K_I is

$$C(K_M, K_I) = \overline{u}\mathrm{div}\overline{u'\mathbf{u}'}+\overline{v}\mathrm{div}\overline{v'\mathbf{u}'}-\frac{\tan\phi}{a}(\overline{u}\,\overline{u'v'}-\overline{v}\,\overline{u'u'}),$$

where ϕ is the latitude. The dissipation of K_M due to friction is

$$D(K_M).$$

The three-dimensional transport of K_M and mean potential energy by the BC is given by

$$B(K_M) = \mathrm{div}\left[\left(\frac{\overline{u}^2+\overline{v}^2}{2}+\overline{\Phi}\right)\overline{\mathbf{u}}\right].$$

The diabatic production/extinction of A_T is

$$G(\overline{A_T}) = \gamma\overline{T'Q'}.$$

The baroclinic energy conversion of the eddy flow is denoted by

$$C(\overline{A_T}, \overline{K_T}) = -\overline{\omega'\alpha'}.$$

The energy conversion between A_T and A_I is

$$C(\overline{A_T}, A_I) = C_p(p/p_0)^{2\kappa}\gamma\overline{\theta'\mathbf{u}'}\cdot\mathrm{grad}(\overline{\theta}-\langle\overline{\theta}\rangle),$$

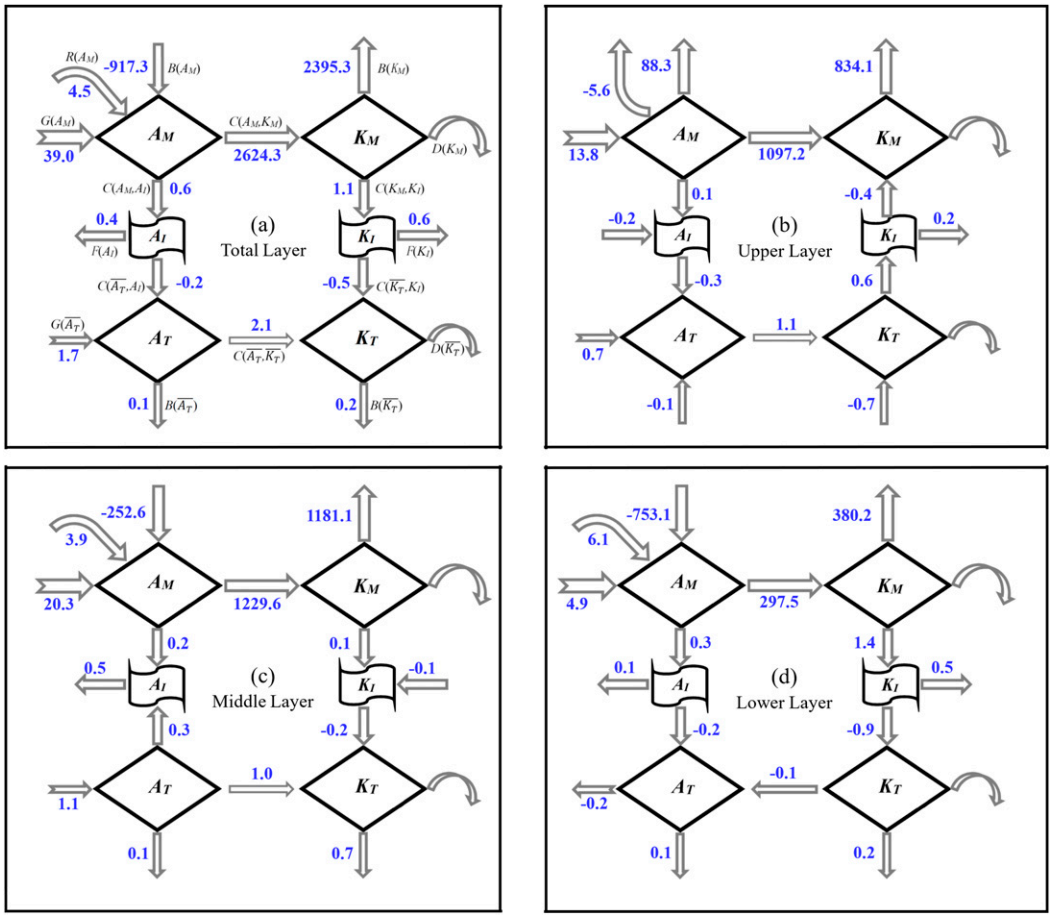

FIG. B1. Vertical integral of the target-region averaged budget terms of Eqs. (1)–(4) (blue values; W m^{-2}) among different layers, where the total, upper, middle, and lower layers have the same definitions as those in Fig. 2, the open arrows show the direction of energy conversion, and the curved arrows represent the effects of dissipation terms.

where grad(·) is the gradient operator. The three-dimensional transport of A_T and other related factors by both the BC and eddy flow is denoted by

$$B(\overline{A_T}) = C_p\left(\frac{p}{p_0}\right)^{2\kappa}\gamma\mathrm{div}\left(\frac{\overline{\theta'^2}}{2}\overline{\mathbf{u}} + \frac{\overline{\theta'^2\mathbf{u}'}}{2}\right).$$

The energy conversion between K_T and K_I is

$$C(\overline{K_T}, K_I) = \overline{u'\mathbf{u}'}\cdot\mathrm{grad}\overline{u} + \overline{v'\mathbf{u}'}\cdot\mathrm{grad}\overline{v} + \frac{\tan\phi}{a}(\overline{u}\,\overline{u'v'} - \overline{v}\,\overline{u'u'}).$$

The dissipation of K_T due to friction is

$$D(\overline{K_T}).$$

Finally, we denote the three-dimensional transport of K_T by the BC and the three-dimensional transport of K_T and perturbation potential energy by the eddy flow by

$$B(\overline{K_T}) = \mathrm{div}\left(\frac{\overline{u'^2} + \overline{v'^2}}{2}\overline{\mathbf{u}}\right) + \mathrm{div}\left[\overline{\left(\frac{u'^2 + v'^2}{2} + \Phi'\right)\mathbf{u}'}\right].$$

The relationships associated with A_I and K_I are $C(A_M, A_I) + C(\overline{A_T}, A_I) - F(A_I) = 0$ and $C(K_M, K_I) + C(\overline{K_T}, K_I) - F(K_I) = 0$, where $F(A_I) \approx \mathrm{div}(\overline{A_I\mathbf{u}'})$ and $F(K_I) = \mathrm{div}(\overline{K_I\mathbf{u}'})$ represent the three-dimensional transport of A_I and K_I, respectively.

APPENDIX B

Calculation Results of the Energy Budget Terms

The detailed energy budget terms of Eqs. (1)–(4) are horizontally averaged within the target region to show the overall characteristics of the precipitation region,

and then the horizontal-mean results are vertically integrated in different layers to represent the total features in the corresponding layers. The results are shown in Fig. B1, and Fig. 2 is a schematic illustration of it.

REFERENCES

Bao, M., 2007: The statistical analysis of the persistent heavy rain in the last 50 years over China and their backgrounds on the large scale circulation (in Chinese). *Chin. J. Atmos. Sci.*, **31**, 779–792.

Chen, F., and J. Dudhia, 2001: Coupling an advanced land surface–hydrology model with the Penn State–NCAR MM5 modeling system. Part I: Model implementation and sensitivity. *Mon. Wea. Rev.*, **129**, 569–585, https://doi.org/10.1175/1520-0493(2001)129<0569:CAALSH>2.0.CO;2.

Chen, Y., and P. Zhai, 2015: Synoptic-scale precursors of the East Asia/Pacific teleconnection pattern responsible for persistent extreme precipitation in the Yangtze River valley. *Quart. J. Roy. Meteor. Soc.*, **141**, 1389–1403, https://doi.org/10.1002/qj.2448.

Davis, C. A., and W. Lee, 2012: Mesoscale analysis of heavy rainfall episodes from SoWMEX/TiMREX. *J. Atmos. Sci.*, **69**, 521–537, https://doi.org/10.1175/JAS-D-11-0120.1.

Ding, Y., 1993: *Study on the Lasting Heavy Rainfalls over the Yangtze-Huaihe River Basin in 1991* (in Chinese). China Meteorological Press, 255 pp.

Duchon, C. E., 1979: Lanczos filtering in one and two dimensions. *J. Appl. Meteor.*, **18**, 1016–1022, https://doi.org/10.1175/1520-0450(1979)018<1016:LFIOAT>2.0.CO;2.

Erlebacher, G., M. Y. Hussaini, and L. Jameson, 1996. *Wavelets: Theory and Applications*. Oxford University Press, 528 pp.

Fu, S.-M., W.-L. Li, and J. Ling, 2015: On the evolution of a long-lived mesoscale vortex over the Yangtze River basin: Geometric features and interactions among systems of different scales. *J. Geophys. Res. Atmos.*, **120**, 11 889–11 917, https://doi.org/10.1002/2015JD023700.

——, J.-H. Sun, J. Ling, H.-J. Wang, and Y.-C. Zhang, 2016a: Scale interactions in sustaining persistent torrential rainfall events during the mei-yu season. *J. Geophys. Res. Atmos.*, **121**, 12 856–12 876, https://doi.org/10.1002/2016JD025446.

——, H.-J. Wang, J.-H. Sun, and Y.-C. Zhang, 2016b: Energy budgets on the interactions between the mean and eddy flows during a persistent heavy rainfall event over the Yangtze River valley in summer 2010. *J. Meteor. Res.*, **30**, 513–527, https://doi.org/10.1007/s13351-016-5121-3.

Hitchens, N. M., H. E. Brooks, and R. S. Schumacher, 2013: Spatial and temporal characteristics of heavy hourly rainfall in the United States. *Mon. Wea. Rev.*, **141**, 4564–4575, https://doi.org/10.1175/MWR-D-12-00297.1.

Holton, J. R., 2004: *An Introduction to Dynamic Meteorology*. Academic Press, 552 pp.

Hong, S.-Y., and J.-O. Lim, 2006: The WRF single-moment microphysics scheme (WSM6). *J. Korean Meteor. Soc.*, **42**, 129–151.

Kain, J. S., 2004: The Kain–Fritsch convective parameterization: An update. *J. Appl. Meteor.*, **43**, 170–181, https://doi.org/10.1175/1520-0450(2004)043<0170:TKCPAU>2.0.CO;2.

Karl, T. R., and R. W. Knight, 1998: Secular trends of precipitation amount, frequency, and intensity in the United States. *Bull. Amer. Meteor. Soc.*, **79**, 231–241, https://doi.org/10.1175/1520-0477(1998)079<0231:STOPAF>2.0.CO;2.

Kuo, H. L., 1974: Further studies of the parameterization of the influence of cumulus convection on large-scale flow. *J. Atmos. Sci.*, **31**, 1232–1240, https://doi.org/10.1175/1520-0469(1974)031<1232:FSOTPO>2.0.CO;2.

Li, D., J. Sun, S. Fu, J. Wei, S. Wang, and F. Tian, 2015: Spatio-temporal characteristics of hourly precipitation over central eastern China during the warm season of 1982–2012. *Int. J. Climatol.*, **36**, 3148–3160, https://doi.org/10.1002/joc.4543.

Li, J., J. Mao, and G. Wu, 2014: A case study of the impact of boreal summer intraseasonal oscillations on Yangtze rainfall. *Climate Dyn.*, **44**, 2683–2702, https://doi.org/10.1007/s00382-014-2425-9.

Liu, G., and R. Wu, 2016: Spatial and temporal characteristics of summer precipitation events spanning different numbers of days over Asia. *Int. J. Climatol.*, **36**, 2288–2302, https://doi.org/10.1002/joc.4495.

Liu, H.-B., J. Yang, D.-L. Zhang, and B. Wang, 2014: Roles of synoptic to quasi-biweekly disturbances in generating the summer 2003 heavy rainfall in east China. *Mon. Wea. Rev.*, **142**, 886–904, https://doi.org/10.1175/MWR-D-13-00055.1.

Liu, R., J. Sun, J. Wei, and S. Fu, 2016: Classification of persistent heavy rainfall events over south China and associated moisture source analysis. *J. Meteor. Res.*, **30**, 678–693, https://doi.org/10.1007/s13351-016-6042-x.

Mao, J., and G. Wu, 2006: Intraseasonal variations of the Yangtze rainfall and its related atmospheric circulation features during the 1991 summer. *Climate Dyn.*, **27**, 815–830, https://doi.org/10.1007/s00382-006-0164-2.

Markowski, P., and Y. Richardson, 2010: *Mesoscale Meteorology in Midlatitudes.* Wiley-Blackwell, 407 pp.

Murakami, S., 2011: Atmospheric local energetics and energy interactions between mean and eddy fields. Part I: Theory. *J. Atmos. Sci.*, **68**, 760–768, https://doi.org/10.1175/2010JAS3664.1.

Noh, Y., W. G. Cheon, and S. Raasch, 2001: The improvement of the K-profile model for the PBL using LES. Preprints, *Int. Workshop of Next Generation NWP Model*, Seoul, South Korea, Laboratory for Atmospheric Modeling Research, 65–66.

Saha, S., and Coauthors, 2014: The NCEP Climate Forecast System version 2. *J. Climate*, **27**, 2185–2208, https://doi.org/10.1175/JCLI-D-12-00823.1.

Schumacher, R. S., and R. H. Johnson, 2006: Characteristics of U.S. extreme rain events during 1999–2003. *Wea. Forecasting*, **21**, 69–85, https://doi.org/10.1175/WAF900.1.

Skamarock, W. C., and Coauthors, 2008: A description of the Advanced Research WRF version 3. NCAR Tech. Note NCAR/TN-475+STR, 113 pp., http://dx.doi.org/10.5065/D6DZ069T.

Tao, S.-Y., 1980: *Rainstorms in China.* Science Press, 225 pp.

Wang, H.-J., J.-H. Sun, J. Wei, and S.-X. Zhao, 2014: Classification of persistent heavy rainfall events over southern China during recent 30 years (in Chinese). *Climatic Environ. Res.*, **19**, 713–725.

Wang, Q.-W., and Z.-M. Tan, 2014: Multi-scale topographic control of southwest vortex formation in Tibetan Plateau region in an idealized simulation. *J. Geophys. Res. Atmos.*, **119**, 11 543–11 561, https://doi.org/10.1002/2014JD021898.

Yamada, T. J., D. Takeuchi, M. A. Farukh, and Y. Kitano, 2016: Climatological characteristics of heavy rainfall in northern Pakistan and atmospheric blocking over western Russia. *J. Climate*, **29**, 7743–7754, https://doi.org/10.1175/JCLI-D-15-0445.1.

Yang, H., and C. Li, 2003: The relation between atmospheric intraseasonal oscillation and summer severe flood and drought in the Changjiang–Huaihe River basin. *Adv. Atmos. Sci.*, **20**, 540–553, https://doi.org/10.1007/BF02915497.

Zhang, Y., J. Sun, and S. Fu, 2016: Main energy paths and energy cascade processes of the two types of persistent heavy rainfall events over the Yangtze River–Huaihe River basin. *Adv. Atmos. Sci.*, **34**, 129–143, https://doi.org/10.1007/s00376-016-6117-8.

Zhao, S.-X., and Coauthors, 2004: *Study on Mechanism of Formation and Development of Heavy Rainfalls on Meiyu Front in Yangtze River*. China Meteorological Press, 282 pp.